

# Pulsar spin-down luminosity: Simulations in general relativity

Milton Ruiz<sup>1,\*</sup>, Vasileios Paschalidis<sup>1,†</sup> and Stuart L. Shapiro<sup>1,2‡</sup>

<sup>1</sup>*Department of Physics, University of Illinois at Urbana-Champaign, Urbana, IL 61801*

<sup>2</sup>*Department of Astronomy & NCSA, University of Illinois at Urbana-Champaign, Urbana, IL 61801*

Adopting our new method for matching general relativistic, ideal magnetohydrodynamics to its force-free limit, we perform the first systematic simulations of force-free pulsar magnetospheres in general relativity. We endow the neutron star with a general relativistic dipole magnetic field, model the interior with ideal magnetohydrodynamics, and adopt force-free electrodynamics in the exterior. Comparing the spin-down luminosity to its corresponding Minkowski value, we find that general relativistic effects give rise to a modest enhancement: the maximum enhancement for  $n = 1$  polytropes is  $\sim 23\%$ . Evolving a rapidly rotating  $n = 0.5$  polytrope we find an even greater enhancement of  $\sim 35\%$ . Using our simulation data, we derive fitting formulas for the pulsar spin-down luminosity as a function of the neutron star compaction, angular speed, and dipole magnetic moment. We expect stiffer equations of state and more rapidly spinning neutron stars to lead to even larger enhancements in the spin-down luminosity.

PACS numbers: 04.25.D-, 04.30.Db, 04.40.Nr 95.30.Sf

## I. INTRODUCTION

Pulsars are believed to be rapidly rotating neutron stars (NSs) that lose their rotational kinetic energy primarily due to emission of electromagnetic radiation (see e.g. [1]). Pulsars are extremely accurate clocks that can be used to probe fundamental physics, such as the nuclear equation of state (EOS), and theories of gravity (see e.g. [2]). They can even function as detectors of gravitational waves [3].

Pulsars are detectable from radio to gamma-ray frequencies. However, only a small number of pulsars is observable in the visible bands [4]. Fermi-LAT technology [5] has allowed the recent discovery of numerous gamma-ray pulsars. To date there are over 2300 known pulsars [6] of which over 130 are gamma-ray pulsars [7, 8]: the vast majority of pulsars are radio pulsars. The most slowly rotating pulsar is PSR-J2144-3933 [9], with a period of 9.43 s. The most rapidly rotating pulsar is PSR-J1748-2446ad [10], with a period of 1.395 ms. Hence pulsar periods cover almost 4 orders of magnitude.

A complete theory that can explain both the radio and the gamma-ray emission remains elusive. Nevertheless, our understanding of pulsar physics has been drastically improved in recent years as a result of computational simulations that model the global pulsar magnetosphere.

Rapid rotation in pulsars induces strong electric fields capable of stripping matter off the NS surface and eventually populating the exterior with tenuous plasma [11]. Motivated by this result, most global studies of pulsar magnetospheres adopt the force-free (FFE) limit of magnetohydrodynamics (MHD), which is valid in such environments. Moreover, to simplify the analysis further,

most studies consider the case where the NS dipole magnetic moment is aligned or antialigned with its angular momentum. This simple model has been successful in producing the main features of the pulsar magnetosphere of an aligned rotator: (i) a near or closed zone, which corotates with the star, and in which magnetic field lines return to the stellar surface; (ii) a far or open zone, which extends beyond the light cylinder radius  $R_{LC}$ , and in which the magnetic lines are open and extend to infinity; (iii) a Y point at the location of the light cylinder, at which the magnetic field lines first open; and (iv) an equatorial current sheet. All these features are predictions of the so-called pulsar equation [12, 13].

The first successful numerical solution of the pulsar equation was presented in [14], which was later followed by numerous studies [15–21] that probed the global features of an aligned rotator in flat spacetime and reinforced the global picture outlined above. These studies did not include the magnetized NS interior and modeled the effects of rotation through a boundary condition on the spherical stellar surface. Simulations of force-free magnetospheres have produced important results, such as a proof of existence of a stationary force-free magnetospheric configuration, the calculation of the spin-down luminosity of force-free oblique rotators [17], and the evolution of the obliquity angle [22], all in flat spacetime. Recently, there have also been some analytic efforts to understand the emission from an accelerated isolated pulsar in flat spacetime (see e.g. [23, 24]).

In addition to assuming that pulsars possess dipole magnetic fields, the common assumptions and simplifications in these earlier studies have been the following:

1. The pulsar magnetosphere is well described by force-free electrodynamics.
2. The backreaction of the magnetic field onto the interior matter is ignored.
3. Deviations from sphericity of the stellar surface (e.g. due to rapid rotation) are ignored.

---

\* ruizm@illinois.edu

† vpaschal@illinois.edu

‡ slshapir@illinois.edu

#### 4. Curved spacetime effects are ignored.

For determining the pulsar spin-down luminosity, assumption 1 is further justified by new results reported in [25], where a particle-in-cell simulation of the global pulsar magnetosphere yields a spin-down luminosity consistent with earlier force-free studies [17]. While assumption 2 is likely to break down in a thin layer near the stellar surface [26–28], the calculations reported in [29] indicate that the backreaction of the magnetic field can lead only to small corrections to the spin-down luminosity. To our knowledge the extent to which assumption 3 is correct has never been studied before (likely due to the complexity of imposing boundary conditions on a nonspherical stellar surface). Relaxing assumption 4 has been argued to lead to important effects. For example, [30] pointed out that general relativity (GR) can amplify the induced electric field due to the rotation of the star. It has also been argued [31, 32] that frame dragging induces an enhanced electric field which contributes to particle acceleration in the polar cap region. More recently, the *vacuum* Maxwell equations were solved in the curved spacetime of a *slowly* rotating NS endowed with a dipole magnetic field [33]. It was shown that GR results in an enhancement in the spin-down luminosity of a pulsar in vacuum up to  $\sim 34\%$  (see also [34] for an earlier analytic study). Furthermore, adopting a GR resistive MHD scheme, it has been reported that the spin-down luminosity from a GR aligned rotator deviates from the corresponding flat spacetime value by  $\sim 20\%$  [29]. As noted in [29] this deviation could be due to the adopted resistive MHD scheme, to the way the flat spacetime spin-down luminosity formula is applied when dealing with oblate stars or to GR effects. The origin of the difference could also be due to the inclusion of backreaction of the magnetic fields onto the thin layer near the NS surface or some combination of all these factors. Finally, force-free simulations of rotating and nonrotating, collapsing neutron stars have recently been performed in [35]. All these earlier studies indicate that GR plays an important role in pulsar magnetospheres.

In this paper we perform the first systematic study of general relativistic effects in the force-free pulsar magnetospheres of aligned rotators. We adopt ideal GRMHD for the NS interior, and model its magnetosphere by adopting general relativistic force-free electrodynamics. Using the numerical method we presented and tested in [36] we match the ideal MHD dense interior to the force-free exterior. We evolve the stars until the systems relax and compute the spin-down luminosity after steady state has been achieved. As in most previous studies we neglect the back-reaction of the magnetic field onto the matter interior. Consequently, all our results scale with the magnetic field strength (or the dipole magnetic moment).

We split our study into two stages: in the first stage we treat the “slow” rotation limit. In particular we generalize the flat spacetime results for the spin-down luminosity by considering sequences of Tolman-Oppenheimer-

Volkoff (TOV) spherical stars, endowing these stars with a slow, uniform, rotational velocity, and a general relativistic dipole magnetic field [37]. When both  $T/|W| \ll 1$  and  $\mathcal{M}/|W| \ll 1$ , where  $T$ ,  $\mathcal{M}$  and  $|W|$  are the kinetic, magnetic and gravitational binding energies, respectively, the stellar structure remains unaffected and nearly spherical. These simulations allow us to isolate and quantify the effects of the *compaction* on the pulsar spin-down luminosity, as frame dragging is not present. We find that the higher the compaction, the larger the enhancement in the spin-down luminosity when compared to its flat spacetime value. The maximum enhancement reaches  $\sim 9.3\%$  near the maximum compaction limit.

In the second stage, we treat the “rapid” rotation limit by constructing self-consistent equilibrium sequences of uniformly rotating, polytropic NSs using the Cook-Shapiro-Teukolsky (CST) code [38, 39]. Endowing these stars with a general relativistic dipole magnetic field (assuming  $\mathcal{M}/|W| \ll 1$ , hence leaving the nonspherical structure of the rotating star unaffected by the magnetic field) and evolving until relaxation, we find that rotation (frame dragging) increases the enhancement of the spin-down luminosity over the corresponding Minkowski value even further. The maximum enhancement for  $n = 1$  polytropes is  $\sim 23\%$ . Evolving a rapidly rotating  $n = 0.5$  polytrope we find an even greater enhancement of  $\sim 35\%$ . Using our simulation data, we derive fitting formulas for the pulsar spin-down luminosity as a function of the NS compaction, angular speed, and dipole magnetic moment. We argue that general relativistic effects are responsible for the observed enhancement and not the distorted surface of the star by considering the flat spacetime evolution of a highly oblate, magnetized star. We find that the spin-down luminosity in this case is practically the same as for a spherical star. We expect that stiffer equations of state and more rapidly rotating stars should lead to even larger enhancements in the pulsar spin-down luminosity.

This paper is organized as follows. In Sec. II we briefly summarize our numerical method for evolving and matching ideal GRMHD to its force-free electrodynamics (GRFFE) limit. We also present the diagnostics we adopt to monitor these systems. A detailed description of our initial data is presented in Sec. III. A set of tests and results are summarized in Sec. IV, where we also include a resolution study. We conclude in Section V with a summary and a discussion of astrophysical implications. Throughout we adopt geometrized units where  $G = c = 1$ .

## II. NUMERICAL METHOD

We now briefly describe our numerical technique for matching ideal GRMHD to its force-free limit. A detailed description of this technique was presented and tested employing a robust suite of tests in [36, 40]. We also describe the adopted grid hierarchy of our numeri-

cal evolution, as well as the diagnostic quantities used to extract relevant physical information.

### A. Ideal MHD-FFE matching

The force-free approximation can be used when the electromagnetic energy density dominates over the matter energy density, as in the magnetospheres of black holes or NSs. Considering that FFE is a limit of ideal MHD, the ideal MHD equations [see e.g. Eqs. (50)-(53) in [36]] can be used to evolve both a perfectly conducting, dense fluid and an extremely low-density plasma, treating the latter in the force-free approximation. Exploiting this correspondence, we have developed and tested a new numerical scheme for matching dense, ideal MHD stellar interiors to force-free magnetospheric exteriors [36] in GR when the rest-mass density distribution, velocity and the spacetime metric are known (see also [35] for an alternative matching technique). In dense, ideal MHD regions our method simply advects the magnetic field via the magnetic induction equation (the “frozen-in” condition). The interior electric field and the Poynting vector follow from the ideal MHD condition [see e.g. Eq. (A1) in [36]]. The interior fields at the surface of the star are smoothly matched to their force-free exterior values.

The force-free dynamical variables we adopt are the magnetic field  $\mathbf{B}$  and the Poynting vector  $\mathbf{S}$ . In terms of these variables, the force-free constraints  $*F^{\mu\nu}F_{\mu\nu} = 0$  and  $F^{\mu\nu}F_{\mu\nu} > 0$  [41], where  $F_{\mu\nu}$  is the Faraday tensor, become  $\mathbf{S} \cdot \mathbf{B} = 0$  and  $\mathbf{B}^4 - \mathbf{S}^2 > 0$  [36]. The evolution equations for these dynamical variables are written as a set of conservation laws precisely in the same form as the ideal MHD evolution equations [36, 42], so that the same GRMHD infrastructure can be adopted to solve both the ideal MHD and the FFE equations.

When treating pulsars with sufficiently weak magnetic fields ( $\mathcal{M}/|W| \ll 1$ ) the matter and velocity profiles and the spacetime metric can be determined to high approximation by solving the Einstein equations for a stationary gravitational field in axisymmetry, coupled to the equation of hydrostatic equilibrium. Since in this work we assume that the magnetic fields are weak, the background fluid and metric fields are kept fixed and correspond to stationary, axisymmetric, uniformly rotating neutron stars. We thus only need to evolve the electromagnetic fields in these stationary background matter and gravitational fields.

### B. Evolution method

Our force-free formulation is embedded in the Illinois GRMHD adaptive mesh refinement code. This code has been extensively tested and presented in different scenarios involving compact objects and/or electromagnetic fields [43–47]. The force-free module solves the equations of ideal GRMHD/FFE adopting high-resolution shock-

capturing methods. Here we employ PPM reconstruction [48] coupled to the Harten, Lax and van Leer approximate Riemann solver [49].

To enforce the  $\nabla \cdot \mathbf{B} = 0$  constraint, the magnetic induction equation is solved using a vector potential formulation (see [45] for details), coupled to the generalized Lorenz gauge condition we developed in [46]. We choose a damping parameter  $\xi = 1.5/\Delta t$ , where  $\Delta t$  is the time step of the coarsest refinement level. This condition is designed to damp and propagate away spurious electromagnetic gauge modes. The time integration of all evolution equations is carried out using a fourth-order Runge-Kutta scheme.

To simultaneously follow the evolution both in the near and the far zones of the pulsar magnetosphere we adopt a fixed-mesh refinement grid hierarchy. The computational grid in all our simulations consists of seven levels of refinement. The length of each refinement box is  $2.4 R_e \times 2^{7-k}$ , where  $R_e$  is the coordinate equatorial radius of the NS, and  $k = 1, \dots, 7$  indicates the level number. Here, the highest-resolution level corresponds to  $k = 7$ . In a typical simulation the finest level covers the stellar radius by 68 zones. The outer boundary is located approximately twenty NS radii beyond the light cylinder. We set the Courant factor  $\Delta t/\Delta x = 0.45$  for  $k = 6, 7$  and  $\Delta t/\Delta x = 0.45/2^{5-k}$  for  $k = 1, \dots, 5$ .

### C. Diagnostics

We compute the outgoing Poynting luminosity using both the Newman-Penrose scalar  $\phi_2$  and the Poynting vector  $\mathbf{S}$  [40],

$$L \equiv \frac{1}{4\pi} \lim_{r \rightarrow \infty} \int r^2 |\phi_2|^2 d\Omega = \lim_{r \rightarrow \infty} \int r^2 S^{\hat{r}} d\Omega. \quad (1)$$

In all our simulations we compute the Poynting luminosity at several radii between the light cylinder and the outer boundary. We find that the Poynting luminosity converges with increasing radius, and is already close to its asymptotic value for distances between 5 and 10 light-cylinder radii from the NS center. This value is recorded in Tables I and II.

In stationary and axisymmetric spacetimes one can define the angular frequency of the magnetic field lines  $\Omega_F$ , which, within the light cylinder of the pulsar, must equal the angular frequency of the star. Hence, we also monitor  $\Omega_F$ , which is given by [41]:

$$\Omega_F(r, \theta) = \frac{F_{tr}}{F_{r\phi}} = \frac{F_{t\theta}}{F_{\theta\phi}}. \quad (2)$$

## III. INITIAL DATA

To study the effects of GR on the pulsar spin-down luminosity we split our study into two stages: In the first stage we treat slowly rotating NSs and in the second

we consider rapidly rotating stars. Next we describe our initial data.

### A. Slowly rotating stars

The hydrodynamic and metric data we adopt for “slowly” rotating NSs are solutions of the Tolman-Oppenheimer-Volkoff (TOV) equations; see e.g. [1]. Assuming that the star is rotating very slowly ( $T/|W| \ll 1$ ), deviations from these spherical solutions are small and of order  $\mathcal{O}(\Omega^2)$ . To model the stellar rotation we endow these spherical stars with a uniform angular velocity field, in the same spirit as studies of pulsar magnetospheres in flat spacetime. Thus, our “slowly” rotating pulsar study is the GR generalization of spherical pulsar magnetospheres in Minkowski spacetime.

For a given angular speed and dipole magnetic moment, our simulations of magnetospheres depend solely on the compaction  $C \equiv M/R$  of the slowly rotating spherical star, where  $M$  is the gravitational (ADM) mass of the star and  $R$  its areal radius. In other words, for a given  $C$  we can use *any* equation of state to determine the interior metric and hydrodynamic fields and obtain the *same* spin-down luminosity. This is expected because a) in GR, the spacetime outside a spherical star of compaction  $C$  is the same, independent of the interior metric and structure, b) the stars are slowly rotating so that the light cylinder radius is much larger than the stellar radius, and its boundary lies in the flat spacetime regime, and c) the magnetosphere within the light-cylinder corotates with the star, preserving its dipole magnetic field structure. Using  $n = 0.5$  and  $n = 1$  polytropic TOV models, we have confirmed our expectation that the calculated spin-down luminosity is independent of the interior model for the NS, and depends only on the value of  $C$ . Thus, we adopt a sequence of (analytic) incompressible TOV stars (see e.g. [1]) which allow us to easily sample the allowed range of stellar compactions for TOV stars.

Table I summarizes the parameters of the sequence of incompressible stars we consider in this study. Note that, as the compaction of the star increases toward the maximum value  $4/9 (= 0.44\bar{4})$ , the central pressure and metric begin to blow up, and when  $C = 4/9$  the spacetime becomes singular [1].

Following [36], we endow these stars with a uniform angular velocity

$$v^\phi \equiv \frac{d\phi}{dt} = \Omega = \text{constant}, \quad (3)$$

where  $\Omega$  is the angular velocity measured at infinity. Deviations from strict hydrostatic equilibrium for these configurations are small since  $\mathcal{M}/|W| \ll 1$  and  $T/|W| \ll 1$ . Adopting TOV solutions allows us to isolate and quantify the effects of the compaction on the pulsar spin-down luminosity, as frame dragging is not accounted for in the metric.

TABLE I. Properties of TOV stars. We list the compaction of the star  $C = M/R$ , the redshift  $Z_p$  of a photon emitted at the pole and measured by a static observer at infinity, and the spin-down luminosity  $L$ , in units of the spin-down luminosity of a force-free aligned rotator in flat spacetime  $L_0 = 1.02 \mu^2 \Omega^4$ .

$C$	$Z_p$	$L/L_0$
0	0	1.0
0.020	0.209	1.018
0.080	0.091	1.048
0.126	0.156	1.067
0.153	0.201	1.077
0.211	0.315	1.085
0.337	0.750	1.091
0.398	0.120	1.093

We choose the angular velocity such that the expected location of the light cylinder radius  $R_{\text{LC}} = 1/\Omega$  is ten NS radii from the NS center. As the inner magnetosphere ( $r_\perp = r \sin \theta \leq R_{\text{LC}}$ ) corotates with the star, the angular velocity of the magnetic field lines  $\Omega_F$  must equal  $\Omega$  in this region. As a result the light cylinder in GR can be computed by finding the locus of points where the speed of the magnetosphere, as measured, say, by a normal observer, equals the speed of light. It is thus the cylindrical surface on which the Lorentz factor  $\Gamma = -n_\alpha u^\alpha$  blows up, where  $n^\alpha$  is the unit timelike vector normal to  $t = \text{const.}$  slices and  $u^\alpha$  the four-velocity corresponding to  $v^\phi$ . The condition  $\Gamma \rightarrow \infty$  gives

$$1 = \frac{\gamma_{ij} (v^i + \beta^i) (v^j + \beta^j)}{\alpha^2}, \quad (4)$$

where  $\gamma_{ij}$ ,  $\alpha$  and  $\beta^i$  are the spatial metric, lapse function and shift vector, respectively, defined through the 3+1 decomposition of the spacetime metric

$$ds^2 = g_{\mu\nu} dx^\mu dx^\nu = -\alpha^2 dt^2 + \gamma_{ij} (dx^i + \beta^i dt) (dx^j + \beta^j dt). \quad (5)$$

As our spacetimes are asymptotically flat, at large distance  $R \ll r$ , we have  $\alpha \rightarrow 1$ ,  $\beta^i \rightarrow 0$ , and  $\gamma_{ij} \rightarrow \delta_{ij}$ , and Eq. (4) reduces to the well-known flat spacetime result  $R_{\text{LC}} = 1/\Omega$  for the light-cylinder radius.

Choosing the angular velocity such that  $R_{\text{LC}} = 10 R$  makes the computations tractable and is roughly consistent with our approximation of slow rotation for the majority of the models we consider here. The ratio of the centrifugal to the gravitational acceleration at the equator is

$$\frac{a_c}{a_g} \approx \frac{T}{|W|} \approx \frac{\Omega^2 R}{M/R^2} = \frac{\Omega^2 R^3}{M} = 0.01 C^{-1}. \quad (6)$$

For TOV stars with  $C \gtrsim 0.15$ ,  $T/|W| \lesssim 6\%$ , hence most of our stars, and especially the very high compaction

ones, are slowly rotating. While the lower compaction stars are not so slowly rotating, the rotation rate is sufficiently slow that the light-cylinder radius is in the asymptotically flat regime, and our slow-rotation study is simply meant to serve as a generalization to the flat spacetime results.

### B. Rapidly rotating stars

The hydrodynamic and metric data for our rapidly rotating compact stars correspond to equilibrium models of uniformly rotating relativistic NSs generated by the Cook-Shapiro-Teukolsky (CST) code [38, 39]. We adopt a polytropic equation of state

$$P = K \rho_0^{1+1/n}, \quad (7)$$

where  $P$  is the pressure,  $\rho_0$  the rest-mass density, and  $K$  and  $n$  are the polytropic constant and index, respectively.

We perform our calculations of rapidly rotating stars in polytropic units, employing dimensionless quantities as in [38, 39]:

$$\bar{M} = K^{-n/2} M, \quad \bar{\Omega} = K^{n/2} \Omega, \quad (8)$$

$$\bar{x}^i = K^{-n/2} x^i, \quad \bar{t} = K^{-n/2} t, \quad \bar{\mu} = K^{-n} \mu, \quad (9)$$

where  $M$  is the mass,  $x^i$  are the spatial coordinates,  $t$  is the time coordinate, and  $\mu$  the dipole magnetic moment. Our calculations scale with  $K$ , which can be set equal to unity in our code.

We construct constant  $\bar{\Omega}$  sequences with polytropic index  $n = 1$ . Table II summarizes the main parameters of the rotating NS models we consider here. Each constant  $\bar{\Omega}$  sequence consists of models that range from the mass-shedding limit to the maximum compaction configuration for the given  $\bar{\Omega}$ . Models at the mass-shedding limit are highly oblate, whereas the deviation from sphericity of models near maximum compaction is small. We also consider the ‘‘supramassive’’ NS limit for  $n = 1$  [39], and a rapidly rotating  $n = 0.5$  model. A supramassive NS is the maximum mass NS configuration for a given equation of state when allowing for uniform rotation. For  $n = 1$  such a configuration exceeds the maximum mass of a nonrotating star by  $\lesssim 20\%$ .

### C. Electromagnetic fields

Flat spacetime studies of pulsar magnetospheres initialize the exterior NS magnetic field to a dipole magnetic field that is a solution of the *vacuum* Maxwell equations. Similarly, we assume that our GR stars possess an exterior dipole magnetic field that at  $t = 0$  is a solution to the vacuum Maxwell equations in Schwarzschild spacetime. The corresponding toroidal vector potential

in Schwarzschild coordinates is given by [37]:

$$A_\phi = \frac{3\mu \sin^2 \theta}{4M} \left[ 1 + \frac{r^2}{2M^2} \ln(1 - 2M/r) + \frac{r}{M} \right], \quad (10)$$

where  $\mu$  is the dipole magnetic moment and  $M$  is the gravitational mass of the NS. We use Eq. (10) to generate the B-field, both in the interior and exterior of the star. Our chosen  $A_\phi$  is the GR generalization of the A-field used in flat spacetime studies of pulsar magnetospheres. Strictly speaking, this generalization is an equilibrium solution only for our spherical stars, because a pure dipole in the vacuum spacetime outside a rapidly rotating NS is not given by Eq. (10). Given that we know of no analytic equilibrium solution for a dipole magnetic field in the vacuum spacetime of a rapidly rotating NS we use Eq. (10) to generate the exterior magnetic field in our rapidly rotating models as well.

We set the initial electric field according to the ideal MHD condition [see Eq. (A1) in [36]]. To guarantee continuity of the electric field across the surface of the star, we set the initial velocity  $u_i$  to be zero in the exterior except for the perpendicular component to the B-field, which we choose to fall off as  $1/r^2$  from its value at the stellar surface. The initial Poynting vector is calculated using

$$S^\mu = -n_\nu T_{EM}^{\mu\nu}, \quad (11)$$

where  $T_{EM}^{\mu\nu}$  is the electromagnetic stress-energy tensor [see e.g. Eq. (15) in [36]].

## IV. RESULTS

In this section we first present a series of additional new tests we performed to check our code, and then we summarize the results from our numerical simulations of the aligned rotator models summarized in Tables. I and II.

### A. Tests and calibration

In [36] we tested our code and GRMHD-FFE matching technique using a suite of robust tests both in flat spacetime and 3D black hole spacetimes. We also reproduced the well-known flat spacetime, aligned rotator solution. To test the robustness of our code even further, and to calibrate our curved spacetime solutions, we performed the following three new tests: i) evolution of a TOV star endowed with a general relativistic dipole magnetic field and no rotation, ii) test of corotation of the inner magnetosphere for a highly compact, slowly rotating TOV star, and (iii) evolution of a highly oblate star in flat spacetime.

TABLE II. Properties of uniformly rotating stars. We list the angular velocity at infinity  $\bar{\Omega}$ , the period in milliseconds,  $M\Omega$ , where  $M$  is the ADM mass, the compaction  $C = M/R$ , where  $R$  is the equatorial circumferential radius, the ratio of the kinetic to the gravitational binding energy  $T/|W|$ , the polar redshift  $Z_p$ , the eccentricity  $e = (1 - R_p/R_e)^{1/2}$ , where  $R_p$  and  $R_e$  are the proper equatorial and polar radii, and the pulsar spin-down luminosity  $L$  in units of its flat spacetime value  $L_0 = 1.02 \mu^2 \Omega^2$ .

$\bar{\Omega}$	Period(ms) <sup>a</sup>	$M\Omega$	$C$	$T/ W $	$Z_p$	$e$	$L/L_0$
0.10 <sup>b</sup>	4.05	0.005	0.030	0.101	0.050	0.828	1.036
		0.009	0.075	0.030	0.094	0.483	1.075
		0.013	0.132	0.012	0.173	0.317	1.096
		0.015	0.161	0.008	0.222	0.263	1.110
		0.016	0.181	0.006	0.261	0.270	1.118
		0.016	0.195	0.005	0.287	0.210	1.122
		0.015	0.244	0.002	0.406	0.136	1.129
0.15 <sup>b</sup>	2.70	0.0147	0.059	0.097	0.104	0.825	1.071
		0.0152	0.072	0.080	0.110	0.730	1.080
		0.0211	0.135	0.028	0.189	0.463	1.115
		0.0243	0.183	0.014	0.272	0.339	1.138
		0.0247	0.221	0.008	0.353	0.257	1.147
		0.0231	0.243	0.004	0.404	0.207	1.149
		0.0273	0.094	0.094	0.170	0.799	1.119
0.20 <sup>b</sup>	2.02	0.0294	0.129	0.056	0.202	0.735	1.139
		0.0318	0.160	0.036	0.245	0.520	1.152
		0.0329	0.180	0.027	0.279	0.458	1.160
		0.0334	0.194	0.022	0.305	0.417	1.165
		0.0333	0.221	0.014	0.360	0.342	1.170
		0.0229	0.243	0.006	0.404	0.250	1.174
		0.38 <sup>b</sup>	1.06	0.070	0.183	0.081	0.403
0.59 <sup>c</sup>	0.84	0.057	0.165	0.136	0.330	0.800	1.357

<sup>a</sup> To assign physical units we choose the polytropic constant  $K$  such that the supramassive limit mass for a given index  $n$  equals the supramassive limit mass of the Akmal - Pandaripandhe - Ravenhall equation of state [50], which is  $2.46M_\odot$  [28].

<sup>b</sup>  $n=1.0$

<sup>c</sup>  $n=0.5$

### 1. TOV star

A straightforward calculation shows that the solution of the *vacuum* Maxwell equations given in Eq. (10) satisfies the three force-free conditions  $F_{\mu\nu}J^\nu = 0$ ,  $*F^{\mu\nu}F_{\mu\nu} = 0$  and  $F^{\mu\nu}F_{\mu\nu} > 0$ . As a result Eq. (10) is also a solution to the general relativistic force-free electrodynamic equations. Consequently, the GRMHD-FFE evolution of a nonrotating TOV star endowed with a dipole magnetic field generated by the vector potential (10) must preserve the initial magnetic field. We have confirmed that this is indeed the case for a star with compaction  $C = 0.174$ . We evolved both the interior and exterior solutions using our code and GRMHD-FFE matching technique and found that the initial solution

is preserved. In Fig. 1 we plot the poloidal magnetic fields at  $t/M = 0$  and  $t/M = 442$ , which corresponds to  $2/3$  of an Alfvén crossing time across the computational domain, and demonstrate that the two fields overlap as expected.

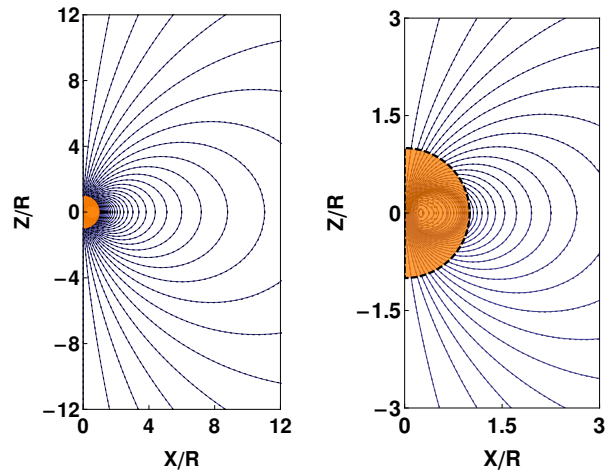


FIG. 1. Poloidal magnetic field lines for a nonspinning TOV star with compaction  $C = 0.174$  and endowed with a GR dipole magnetic field. The lines at  $t/M = 0$  (black dashed curves) overlap the field lines at  $t/M = 442$  (blue solid curves). The time  $t/M = 442$  corresponds to  $\sim 2/3$  Alfvén crossing time. Left panel: Far zone magnetic field lines. Right panel: Near zone magnetic field lines.

### 2. Corotation of inner magnetosphere

In all of our evolutions we monitor the angular frequency of the magnetic field lines  $\Omega_F$  computed via Eq. 2. To demonstrate that the inner magnetosphere corotates with the star, even for highly curved spacetimes, we show here the level of corotation our code achieves for a TOV star with compaction  $C = 0.33$  (see Table I).

Figure 2 plots  $\Omega_F$  on the  $x - z$  plane as a function of the polar angle  $\theta$  at  $r = 0.2R_{LC}$  and  $r = 0.5R_{LC}$  at two different resolutions covering the stellar radius by 68 and 130 zones, respectively. Here  $r$  is the coordinate radius. It is clear that the magnetosphere corotates with the star even for such high compactions. Notice also that the higher the resolution the higher the degree of corotation, as expected from earlier results we reported in flat spacetime [36]. Similar levels of corotation are achieved for all models we consider here.

### 3. Evolution of an oblate star in flat spacetime

To quantify the effects of the shape of the stellar surface on the structure of the magnetosphere and the spin-down luminosity we evolve a highly oblate neutron star

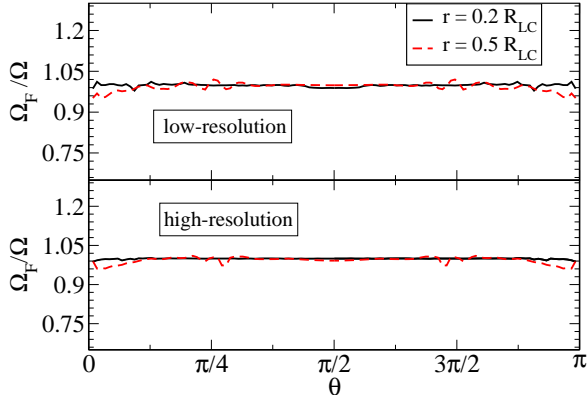


FIG. 2. Angular frequency of the magnetic field lines  $\Omega_F$  normalized by the angular velocity of the star  $\Omega$  as a function of the polar angle in the  $x-z$  plane at  $r = 0.2 R_{LC}$  and  $r = 0.5 R_{LC}$  for a TOV star with  $C = 0.33$ . Two different resolutions are shown (low and high). As expected, the magnetosphere within the light cylinder  $R_{LC}$  corotates with star and the higher the resolution the higher is the degree of corotation.

with eccentricity  $e = (1 - R_p/R_e)^{1/2} = 0.799$ , where  $R_p$  ( $R_e$ ) is the proper polar (equatorial) radius, that corresponds to the shape and spin of the equilibrium model near the mass-shedding limit of the sequence  $\bar{\Omega} = 0.20$  (see Table II). However, we assume a flat spacetime and endow the star with a flat spacetime dipole magnetic field.

The system is evolved until magnetic field relaxation, which occurs after approximately three rotation periods. The relaxed state has the same features as the pulsar magnetosphere of a spherical star, i.e., an inner closed magnetosphere which corotates with the star, an equatorial current sheet, and a  $Y$  point at the location of the light cylinder, beyond which the field lines open. Figure 3 displays the poloidal magnetic field lines at  $t \approx 6\pi/\Omega$  demonstrating the above features.

We find that  $\Omega_F$  is equal to  $\Omega$  at the same level of accuracy as reported in Sec. IV A 2. We find that the pulsar spin-down luminosity is  $L \approx 1.01 L_0$ . Here  $L_0$  is the luminosity we calculate for an independent, high-resolution simulation of a rotating *spherical* star in flat spacetime,

$$L_0 = 1.02 \mu^2 \Omega^4 \simeq 10^{43} B_{12}^2 R_{10}^6 P_{\text{ms}}^{-4} \frac{\text{erg}}{\text{sec}}, \quad (12)$$

where  $B_{12} = B/10^{12}\text{G}$ ,  $R_{10} = R/10\text{km}$  and  $P_{\text{ms}} = P/1\text{ms}$ . Our Eq. (12) is consistent with the value  $L = (1 \pm 0.05) \mu^2 \Omega^4$  reported in [17].

We conclude that for the same  $\Omega$  and  $\mu$  the outgoing Poynting luminosity for an aligned rotator in flat spacetime is essentially independent of the shape of the stellar surface. Notice that this result is not too surprising, since

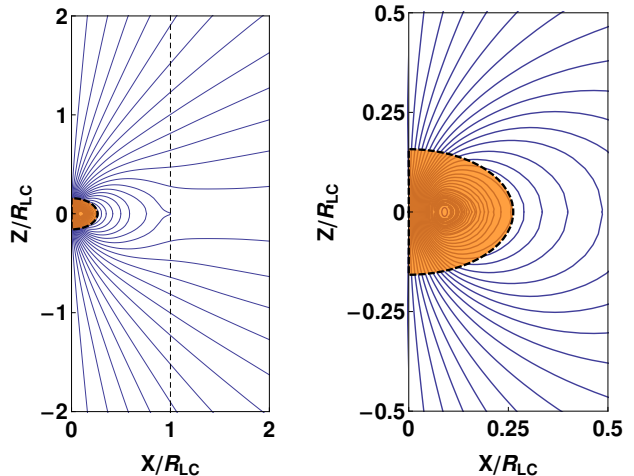


FIG. 3. Poloidal magnetic field lines on the  $x-z$  plane for a rotating neutron star with eccentricity  $e = 0.799$  and angular velocity  $\bar{\Omega} = 0.20$  (see Table II) in flat spacetime after the system has relaxed at  $t \approx 6\pi/\Omega$ . The shaded areas designate the stellar interior. Left panel: Magnetic field lines in the far zone. The dashed vertical line indicates the light cylinder. Right panel: Magnetic field lines in the near zone.

the magnetic field, both in the interior and the exterior inner magnetosphere, corotates with the star, preserving the location of the light cylinder radius beyond which the field lines open and contribute to the outgoing Poynting flux. Therefore, the shape of the stellar surface should not matter and the results should be the same as if the star were a sphere.

This test helps us conclude that deviations from the flat spacetime spin-down luminosity in GR are likely not due to the distorted surface of the star, and motivates our looking elsewhere for GR corrections to the pulsar spin-down luminosity. This is what we do in the following sections.

## B. Slowly rotating sequence

We evolved the sequence of TOV stars presented in Table I until relaxation. We find that the global structure of the magnetosphere has the same features as in flat spacetime (see e.g. Fig. 3) with the main difference being that the light-cylinder radius is now more consistent with Eq. (4), rather than the flat spacetime value given by  $R_{LC} = 1/\Omega$ .

Normalizing the pulsar spin-down luminosity to  $L_0 = 1.02 \mu^2 \Omega^4$ , we find that GR effects enhance the outgoing Poynting luminosity over  $L_0$ . We list the values of  $L/L_0$  for all cases in the last column of Tab. I, and plot  $L/L_0$  vs  $C = M/R$ , where  $M$  is the ADM mass and  $R$  the areal radius of the star, and vs the redshift  $Z_p$  from the stellar surface as measured by static observer at infinity in Fig. 4. As expected, models near the flat spacetime

regime ( $C \rightarrow 0$ ) give rise only to a *small* enhancement of the pulsar spin-down luminosity over  $L_0$ . However, the enhancement increases monotonically with  $C$ , reaching a plateau for  $C \gtrsim 0.35$ . For the maximum compaction model we have considered, the resulting enhancement is approximately 9.3%. As our  $C \approx 0.4$  model is close to the maximum compaction limit for TOV stars ( $C_{\max} = 4/9$ ), we do not expect any further enhancement beyond  $C \approx 0.4$ .

For the TOV sequence we investigated several fitting functions of the form:

$$L = F(C)L_0, \quad (13)$$

for a given  $\Omega$  and  $\mu$ , and found that the following fourth-order polynomial provides an excellent fit to the results of our simulations:

$$F(C) = 1 + 0.78C - 2.16C^2 - 1.77C^3 + 0.55C^4. \quad (14)$$

The right panel in Fig. 4 shows the above fit, where  $C$  is implicitly related to  $Z_p$  by

$$Z_p = \left(1 - \frac{2M}{R}\right)^{-1/2} - 1 = (1 - 2C)^{-1/2} - 1. \quad (15)$$

### C. Rapidly rotating neutron stars

We evolved the rapidly rotating neutron star models listed in Table II until relaxation. The global structure of the magnetosphere in all cases is similar to the flat spacetime one as expected. Figure 5 displays the relaxed poloidal magnetic field lines on the  $x-z$  plane for the ultrastiff, highly distorted  $n = 0.5$  neutron star model (see Table II). The dashed (inner) line indicates the location of the light cylinder calculated in GR via Eq. (4), while the dotted (outer) line corresponds to the value of  $R_{\text{LC}}$  in flat spacetime. The location of the  $Y$  point agrees better with the GR prediction.

Normalizing the pulsar spin-down luminosity  $L$  by  $L_0$  we find that accounting for the stellar rotation self-consistently results in a greater enhancement of  $L$  over  $L_0$  than the values found in the previous section. *The higher the compaction of the star and the more rapidly the star rotates, the larger the enhancement.* The maximum enhancement in  $L$  for each of the  $\bar{\Omega} = 0.10, 0.15, 0.20$  sequences is approximately 13%, 15% and 17%, respectively. The maximum enhancement for  $n = 1$  polytropes we found here is set by the supramassive limit and is 23%. However, changing the stiffness of the equation of state we can achieve greater enhancements. The enhancement in the spin-down luminosity over  $L_0$  for the  $n = 0.5$  model with angular velocity  $\bar{\Omega} = 0.59$  is 35%. Therefore, *we expect stiffer equations of state and more rapidly rotating neutron stars to lead to even larger enhancements.* We list the values of  $L/L_0$  for all cases in the last column of Table II, and plot  $L/L_0$  vs  $C$  and vs  $Z_p$  in Fig. 4 for our  $n = 1$  cases.

For the spin-down luminosity in the  $n = 1$  rapidly rotating cases we investigated fitting functions of the form

$$L = G(Z_p, \bar{\Omega})L_0. \quad (16)$$

We find that the following function

$$G(Z_p, \bar{\Omega}) = 1 + 0.76C(Z_p) - 0.32C(Z_p)^2 + 7.38\bar{\Omega}^2C(Z_p) - 3.53C(Z_p)^3 - 4.75\bar{\Omega}^2C(Z_p)^2, \quad (17)$$

provides an excellent fit to the simulation data. Here  $C(Z_p, \bar{\Omega})$  is an “effective” compaction function defined as in Eq. (15),

Equation (17) has been chosen such that as  $Z_p \rightarrow 0$ ,  $G(Z_p, \bar{\Omega}) \rightarrow 1$ , thereby recovering the flat spacetime result  $L = L_0$ . Moreover, we considered only even powers in  $\bar{\Omega}$  because the resulting spin-down luminosity must not depend on whether the dipole magnetic moment is aligned or antialigned with the spin angular momentum of the star.

### D. Resolution study and error bars

Convergence tests of our GRFFE code and our GRMHD-GRFFE matching method in black hole spacetimes and in black hole-neutron star binaries have already been presented in [36, 40]. Here we perform a convergence test of corotation of the near-zone magnetosphere using our calculations of the supramassive  $n = 1$  NS.

We compute the convergence factor  $c_F$  defined as

$$c_F = \frac{\|u_{\Delta_1}\|}{\|u_{\Delta_2}\|}, \quad (18)$$

at two different resolutions  $\Delta_1 > \Delta_2$ , where we define  $u = 1 - \Omega_F/\Omega$  at  $r/R_{\text{LC}} = 0.5$ , and  $\|\cdot\|$  designates the  $L_2$  norm. Using three different resolutions: the low, medium and high covering the stellar radius by 56, 68 and 85 zones, respectively, we found that the convergence factor is  $c_F = 1.479$ , when high and medium resolutions are used, and  $c_F = 2.127$ , when high and low resolutions are used. These results imply that our code is 1.8-order accurate on average, where the order of convergence  $p$  is determined by solving  $c_F = (\Delta_1/\Delta_2)^p$  for  $p$ .

Studying the spin-down luminosity  $L$  as a function of resolution, we find that  $|(L_{\text{high}} - L_{\text{low}})/L_{\text{high}}| \approx 1\%$ , where  $L_{\text{high}}$  ( $L_{\text{low}}$ ) is the spin-down luminosity in the high (low) resolution. As we have found our results to be convergent we place an error bar on our high-resolution simulations of order 2%. This implies that the deviations from the flat spacetime luminosity we reported in the previous section are real and not due to numerical error.

As pointed out by [20] and [22], some force-free and MHD studies of aligned rotators, have strong numerical dissipation of the Poynting luminosity past the light cylinder. Defining the dissipation of the Poynting luminosity in GR in the same way as in flat spacetime studies



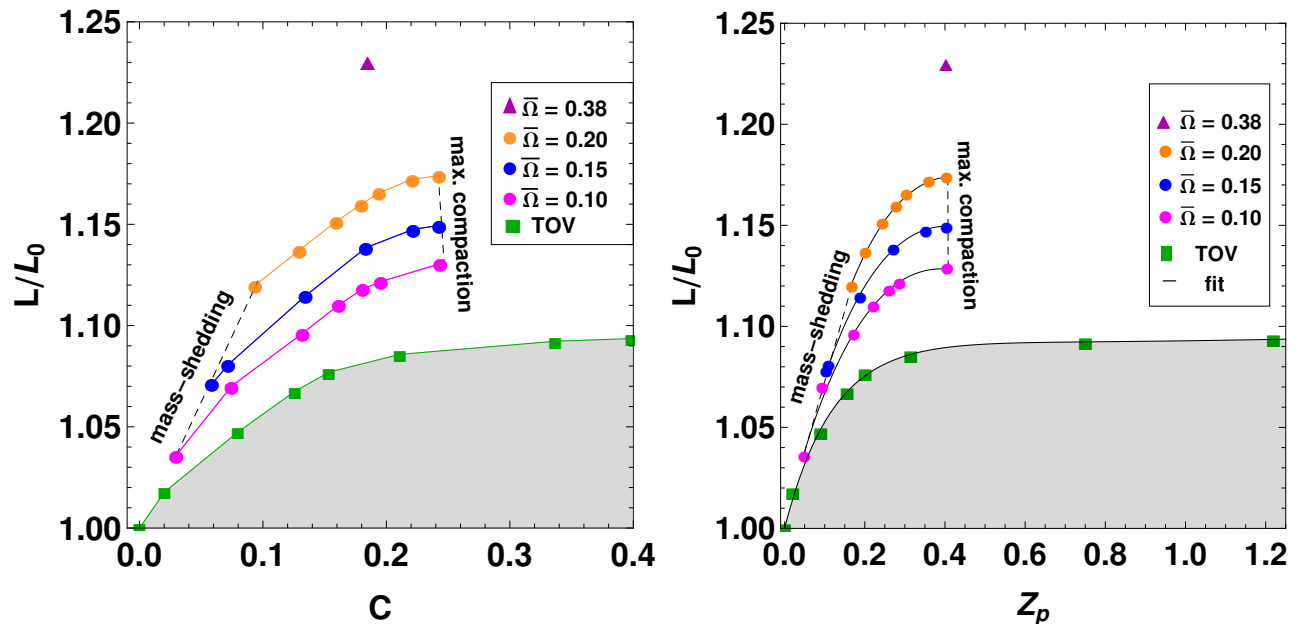


FIG. 4. Pulsar spin-down luminosity  $L$  normalized by  $L_0 = 1.02\mu^2\Omega^4$ , our flat-spacetime result, for models listed in Tables. I and II. Left panel:  $L/L_0$  vs compaction  $C$ . Right panel:  $L/L_0$  vs polar redshift  $Z_p$ , where the points are connected by the fitting functions defined in Eqs. (14)-(17). The parameter space for rotating stars is contained between the left dashed line (the mass-shedding limit) and the right dashed line (maximum compaction). The top point (triangle) corresponds to the supramassive neutron star limit for  $n = 1$ . The lower shaded zone is the area of the parameter space that cannot be reached, unless we assume flat spacetime.

(see e.g. [20]), is not meaningful because of gauge ambiguities that may arise due to calculating the luminosity as a surface integral over a sphere of constant radius in the strong-field regime. To show how much dissipation may exist in our simulations, we plot in Fig. 6 the radial dependence of the Poynting luminosity for a uniformly rotating star with compaction  $C = 0.183$  and angular velocity  $\bar{\Omega} = 0.15$  (see Table II), where the light cylinder is in a regime where the gravitational field is not too strong. Past a radius of 2 light-cylinder radii and out to 10 light-cylinder radii, the luminosity drops only by  $\sim 4\%$ , asymptoting to the value we quote in Table II. It is not entirely clear whether the drop is due to numerical dissipation of the Poynting luminosity, to gauge contributions in the surface integral, or to a combination of the two. However, if it is due to dissipation, the result indicates that the dissipation must be small and near our quoted error bars.

## V. CONCLUSIONS

Magnetized neutron stars possess a force-free magnetosphere. Pulsar magnetospheres have been studied numerically over the last two decades. However, all of these early force-free studies were carried out in flat spacetime. It has been suggested that general relativistic effects may become important but due mainly to frame

dragging [31, 32].

Using the new method we recently developed for matching general relativistic ideal MHD to its corresponding force-free limit, we have performed the first systematic study of aligned rotator force-free magnetospheres in GR. We constructed equilibrium sequences of “slowly” and rapidly rotating NSs. The former are modeled as incompressible TOV stars covering almost the entire allowed range of compaction. The latter are constant  $\Omega$  sequences of uniformly, rapidly rotating, GR, polytropic stars generated by the CST code, and ranging from the mass-shedding limit to the maximum compaction configuration for a given stellar angular frequency  $\Omega$ . We endowed these stars with a weak GR dipole magnetic field and evolved the fields to relaxation.

Some of our rapidly rotating NS models (those close to the mass-shedding limit) are highly distorted (see Table II). To ensure that any deviations from the flat spacetime spin-down luminosity are due to strong field effects and not to the distorted surface of the stars, we evolved a highly oblate star (with eccentricity  $e = 0.799$ ) in flat spacetime, and found that the outgoing Poynting luminosity is independent of the shape of the stellar surface, i.e., the resulting spin-down luminosity is approximately the same as if the star were a sphere spinning with the same angular frequency and endowed with the same magnetic field.

Normalizing the spin-down luminosity  $L$  to its corre-

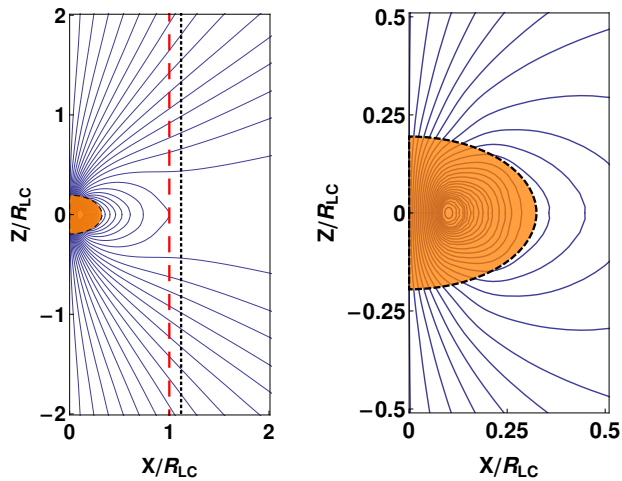


FIG. 5. Poloidal magnetic field lines at the relaxed state of the rapidly rotating  $n = 0.5$  NS model (see Table II). The shaded area designates the stellar interior. Left panel: Far-zone solution. The vertical dashed (dotted) line indicates the GR (flat spacetime) prediction for the location of the light cylinder. Right panel: Near-zone solution. The  $Y$  point coincides with the GR prediction for the location of the light cylinder.

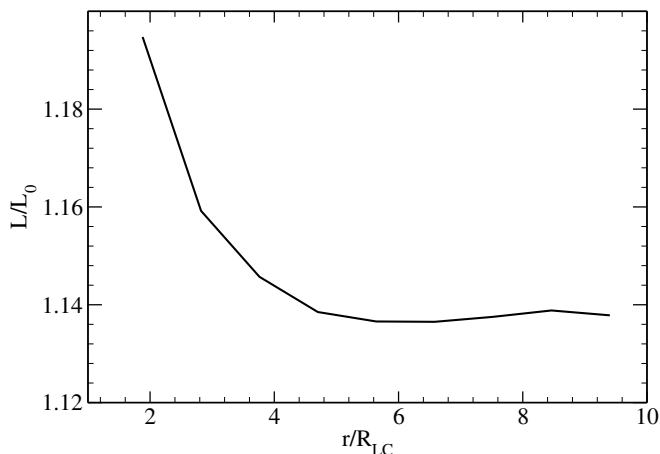


FIG. 6. Radial dependence of the Poynting luminosity  $L/L_0$  for an uniformly rotating star with compaction  $C = 0.183$  and angular velocity  $\bar{\Omega} = 0.15$  (see Table II). Notice that beyond a radius of 2 light-cylinder radii and out to 10 light-cylinder radii, the luminosity drops only by  $\sim 4\%$  which indicates that the dissipation must be small.

sponding Minkowski value  $L_0$ , we find that GR effects give rise to a modest enhancement. As both the compaction and the stellar angular frequency increase, the enhancement becomes more pronounced. In the “slow” rotation limit, where we isolate the effects of compaction, the maximum enhancement is  $\sim 9.3\%$ , independent of the equation of state. However, for rapidly rotating stars, where frame dragging is also important, the maximum

enhancement for  $n = 1$  polytropes is  $\sim 23\%$ , and for a rapidly rotating  $n = 0.5$  polytrope we find an enhancement of  $\sim 35\%$ . We expect stiffer equations of state and more rapidly neutron rotating stars to lead to even larger enhancements in the spin-down luminosity. For the cases we studied here we provided fitting functions for the general relativistic spin-down luminosity of the form  $L = G(Z_p, \Omega)L_0$ , where  $Z_p$  is the gravitational redshift of light emitted from the NS pole as measured by a static observer at infinity.

Our results show that even moderate compaction stars (for which frame dragging is accounted for) have larger  $L/L_0$  than the highest compaction TOV model (for which frame dragging is not accounted for). Hence, it is natural to conclude that there is a strong correlation between frame dragging and the enhancement of the spin-down luminosity over its value in flat spacetime. This suggestion is consistent with the findings of earlier theoretical arguments [31, 32] of why GR pulsar magnetospheres are different than those in flat spacetime. Further studying the source of the differences between GR and flat spacetime studies of pulsars, is beyond the scope of this paper, and will be the subject of a future work.

Should future gravitational wave observations prove able to constrain the nuclear equation of state (see e.g. [51–53] and references therein), our study of pulsar magnetospheres and similar future studies can constrain the NS magnetic field strength and geometry as follows: pulsars in detached, mildly relativistic binaries allow for a determination of the pulsar mass, the angular frequency of rotation, and the spin-down rate. If the nuclear equation of state is known then the compaction of the NS follows from the mass-radius relationship. As the spin-down luminosity depends on the compaction, the angular speed and the magnetic field, then from observations one can constrain the magnetic field, given that all the other parameters are in principle measurable or can be inferred. Even the obliquity angle between the magnetic dipole moment and the rotation axis could possibly be constrained, once oblique rotators are studied in GR. This motivates an investigation of such rotators in GR, which we intend to perform in a future study.

## ACKNOWLEDGMENTS

It is a pleasure to thank Roman Gold for useful discussions. This paper was supported in part by NSF Grants PHY-0963136 and PHY-1300903 as well as NASA Grants NNX11AE11G and NNX13AH44G at the University of Illinois at Urbana-Champaign. VP gratefully acknowledges support from a Fortner Fellowship at UIUC. This work used the Extreme Science and Engineering Discovery Environment (XSEDE), which is supported by NSF grant number OCI-1053575. This research is part of the Blue Waters sustained-petascale computing project, which is supported by the National Science Foundation (award number OCI 07-25070) and the state of Illinois.

Blue Waters is a joint effort of the University of Illinois

at Urbana-Champaign and its National Center for Supercomputing Applications.

- 
- [1] S. L. Shapiro and S. A. Teukolsky, *Black Holes, White Dwarfs, and Neutron Stars* (John Wiley & Sons, New York, 1983)
- [2] D. Psaltis, *Living Reviews in Relativity* **11** (2008), doi:"bibinfo doi 10.12942/lrr-2008-9, <http://www.livingreviews.org/lrr-2008-9>
- [3] G. Hobbs *et al.*, *Classical and Quantum Gravity* **27**, 084013 (2010), <http://stacks.iop.org/0264-9381/27/i=8/a=084013>
- [4] A. Shearer and A. Golden, in *Neutron Stars, Pulsars, and Supernova Remnants*, edited by W. Becker, H. Lesch, and J. Trümper (2002) p. 44, astro-ph/0208579
- [5] W. Atwood *et al.* (LAT Collaboration), *Astrophys.J.* **697**, 1071 (2009), arXiv:0902.1089 [astro-ph.IM]
- [6] R. N. Manchester, G. B. Hobbs, A. Teoh, and M. Hobbs, *Astron. J.* **129**, 1993 (Apr. 2005), astro-ph/0412641
- [7] <https://confluence.slac.stanford.edu/display/GLAMCOG/Public+List+of+LAT-Detected+Gamma-Ray+Pulsars>
- [8] A. Abdo *et al.* (The Fermi-LAT collaboration), *Astrophys.J.Suppl.* **208**, 17 (2013), arXiv:1305.4385 [astro-ph.HE]
- [9] S. Zane, M. Cropper, R. Turolla, L. Zampieri, M. Chieriegato, J. J. Drake, and A. Treves, *Astrophys. J.* **627**, 397 (Jul. 2005), astro-ph/0503239
- [10] J. W. T. Hessels, S. M. Ransom, I. H. Stairs, P. C. C. Freire, V. M. Kaspi, and F. Camilo, *Science* **311**, 1901 (Mar. 2006), astro-ph/0601337
- [11] P. Goldreich and W. H. Julian, *Astrophys. J.* **157**, 869 (1969)
- [12] F. C. Michel, *Astrophys. J. Letters* **180**, L133 (1973)
- [13] E.T. Scharlemann and R.V. Wagoner, *Astrophys. J.* **182**, 951 (1973)
- [14] I. Contopoulos, D. Kazanas, and C. Fendt, *Astrophys.J.* **511**, 351(1999)
- [15] S. S. Komissarov, *ArXiv Astrophysics e-prints*(Nov. 2002), arXiv:astro-ph/0211141
- [16] J. C. McKinney, *Mon.Not.Roy.Astron.Soc.Lett.* **368**, L30 (2006), arXiv:astro-ph/0601411 [astro-ph]
- [17] A. Spitkovsky, *Astrophys. J. Lett.* **648**, L51 (Sep. 2006), arXiv:astro-ph/0603147
- [18] A. Gruzinov, *JCAP* **0811**, 002 (2008), arXiv:0804.4176 [astro-ph]
- [19] A. Gruzinov(2013), arXiv:1303.4094 [astro-ph.HE]
- [20] A. Tchekhovskoy and A. Spitkovsky(2012), arXiv:1211.2803 [astro-ph.HE]
- [21] D. A. Uzdensky and A. Spitkovsky, *Astrophys.J.* **780**, 3 (2014), arXiv:1210.3346 [astro-ph.HE]
- [22] A. Philippov, A. Tchekhovskoy, and J. G. Li(2013), arXiv:1311.1513 [astro-ph.HE]
- [23] T. D. Brennan and S. E. Gralla(2013), arXiv:1311.0752 [astro-ph.HE]
- [24] S. E. Gralla and T. Jacobson(2014), arXiv:1401.6159 [astro-ph.HE]
- [25] A. Philippov and A. Spitkovsky(2013), arXiv:1312.4970 [astro-ph.HE]
- [26] L. Mestel and S. Shibata, *Mon.Not.Roy.Astron.Soc.* **271**, 621 (1994)
- [27] I. Contopoulos, D. Kazanas, and C. Fendt, *Astrophys.J.* **511**, 351 (1999), arXiv:astro-ph/9903049 [astro-ph]
- [28] I. A. Morrison, T. W. Baumgarte, and S. L. Shapiro, *Astrophys.J.* **610**, 941 (2004), arXiv:astro-ph/0401581 [astro-ph]
- [29] C. Palenzuela, *Mon. Not. R. Aston. Soc.* **431**, , 1853 (2), arXiv:1212.0130 [astro-ph.HE]
- [30] Deutsch Arnim J.,, *Annales dAstrophysique* **18**, 1 (1955)
- [31] Beskin, V. S., *Soviet Astronomy Letters* **16**, 286 (1990)
- [32] A. I. Muslimov, A. G.; Tsygan, *Mon.Not.Roy.Astron.Soc.* **255**, 61 (1992)
- [33] J. Pétri(2014), arXiv:1401.1367 [astro-ph.HE]
- [34] L. Rezzolla and B. J. Ahmedov, *Mon.Not.Roy.Astron.Soc.* **352**, 1161 (2004), arXiv:gr-qc/0406018 [gr-qc]
- [35] L. Lehner, C. Palenzuela, S. L. Liebling, C. Thompson, and C. Hanna, *Phys.Rev.* **D86**, 104035 (2012), arXiv:1112.2622 [astro-ph.HE]
- [36] V. Paschalidis and S. L. Shapiro(2013), arXiv:1310.3274 [astro-ph.HE]
- [37] I. Wasserman and S. L. Shapiro, *Astrophys.J.* **265**, 1036 (1983)
- [38] G. B. Cook, S. L. Shapiro, and S. A. Teukolsky*Astrophys.J.* **422**, 227 (1994)
- [39] G. B. Cook, S. L. Shapiro, and S. A. Teukolsky, *Astrophys.J.* **424**, 823 (1994)
- [40] V. Paschalidis, Z. B. Etienne, and S. L. Shapiro, *Phys.Rev.* **D88**, 021504 (2013), arXiv:1304.1805 [astro-ph.HE]
- [41] R. D. Blandford and R. L. Znajek., *Mon. Not. R. Astr. Soc.* **179**, 433 (1977)
- [42] J. C. McKinney, *Mon.Not.Roy.Astron.Soc.* **367**, 1797 (2006), arXiv:astro-ph/0601410 [astro-ph]
- [43] M. D. Duez, Y. T. Liu, S. L. Shapiro, and B. C. Stephens, *Phys.Rev.* **D72**, 024028 (2005), arXiv:astro-ph/0503420 [astro-ph]
- [44] Z. B. Etienne, Y. T. Liu, and S. L. Shapiro, *Phys.Rev.* **D82**, 084031 (2010), arXiv:1007.2848 [astro-ph.HE]
- [45] Z. B. Etienne, V. Paschalidis, Y. T. Liu, and S. L. Shapiro, *Phys.Rev.* **D85**, 024013 (2012), arXiv:1110.4633 [astro-ph.HE]
- [46] B. D. Farris, R. Gold, V. Paschalidis, Z. B. Etienne, and S. L. Shapiro, *Phys. Rev. Lett.* **109**, 221102 (Nov 2012), <http://link.aps.org/doi/10.1103/PhysRevLett.109.221102>
- [47] R. Gold, V. Paschalidis, Z. B. Etienne, S. L. Shapiro, and H. P. Pfeiffer(2013), arXiv:1312.0600 [astro-ph.HE]
- [48] P. Colella and P. R. Woodward, *J. Comput. Phys.* **54**, 174 (1984)
- [49] A. Harten, P. D. Lax, and B. van Leer, *SIAM Rev.* **25**, 35 (1983)
- [50] A. Akmal, V. R. Pandharipande, and D. G. Ravenhall, *Phys. Rev. C* **58**, 1804 (Sep 1998), <http://link.aps.org/doi/10.1103/PhysRevC.58.1804>

- [51] B. D. Lackey, K. Kyutoku, M. Shibata, P. R. Brady, and J. L. Friedman, *Phys.Rev.* **D85**, 044061 (2012), arXiv:1109.3402 [astro-ph.HE]
- [52] A. Bauswein and H.-T. Janka, *Phys.Rev.Lett.* **108**, 011101 (2012), arXiv:1106.1616 [astro-ph.SR]
- [53] V. Paschalidis, Z. B. Etienne, and S. L. Shapiro, *Phys.Rev.* **D86**, 064032 (2012), arXiv:1208.5487 [astro-ph.HE]